

Toward Carbon-Free Cathodes for Fluoride Ion Batteries: Deconvoluting Effects of Active Material and Conductive Additive on Charging and Cyclic Stability

Tommi Hendrik Aalto, Roham Talei, Kathrin Küster, Guido Schmitz, and Oliver Clemens*

In this study, conductive, fluorine and antimony codoped tin oxide nanoparticles (FATO-NPs) are highlighted as a possible alternative for conductive carbon additives in fluoride ion batteries, successfully circumventing oxidative side reactions. Since good cyclability with high and stable discharge capacities is achieved with both types of conductive additive at a high stack

pressure of 180 MPa, it is concluded that conductive carbon is well-suited for high-voltage fluoride ion batteries, contrary to prior assumptions. However, FATO-NP-based cathodes outperform those based on conductive carbon at lower stack pressures of 50 MPa, emphasizing the importance of avoiding carbon fluorination at low stack pressures.

1. Introduction

All-solid-state fluoride ion batteries (ASS-FIBs) are promising candidates for postlithium-ion battery technologies. Many possible combinations of conversion-based anode and cathode materials could outperform current lithium-ion batteries in terms of gravimetric capacity and volumetric energy density.^[1] However, conversion-based materials suffer from rapid capacity fading and poor rate capability due to high volume change and large overpotentials associated with the reorganization of the crystal structure upon conversion.^[2] Therefore, intercalation-based materials, as they are also employed in current state-of-the-art lithium-ion batteries, appear to be the way forward to achieve high cyclic stability for ASS-FIBs.

Earlier publications on intercalation cathode materials for fluoride ion batteries have highlighted fluorination of the conductive carbon additive as a parasitic side reaction leading to rapid deterioration of the cell performance.^[3] Materials, like La_2NiO_4 and La_2CoO_4 , can intercalate fluoride ions in the rocksalt layer

of the Ruddlesden–Popper structure, oxidizing the transition metal ions. Thereby, these materials can store electrical energy reversibly by intercalation and deintercalation of fluoride ions.^[3,4] However, since the fluorination of materials such as $\text{La}_2(\text{Ni}/\text{Co})\text{O}_4$ is happening at potentials very similar to carbon fluorination, the two materials fluorinate simultaneously. Since carbon monofluoride (CF_n), polytetrafluoroethylene (PTFE: $(\text{CF}_2)_n$), and other analogous highly fluorinated carbons are all electronically insulating, the fluorination of the carbon additive was assumed to cause rapid capacity fading as observed by Nowroozi et al.^[3–5] and Wissel et al.^[6] in agreement with observed changes in the carbon oxidation state from X-ray photoelectron spectroscopy (XPS) studies.

To differentiate the fluorination of $\text{La}_2(\text{Ni}/\text{Co})\text{O}_4$ from the conductive additive, one option is to replace carbon by other conductive materials which show higher oxidative stability. Conductive oxides could serve the purpose, since the metals contained are already oxidized to their highest oxidation state, leaving no option for further oxidation by electrochemical fluorination apart from the oxidation of lattice oxygen. Especially, SnO_2 -based conductive oxides are prominent due to the vast amounts of literature on those materials, due to their application as transparent conductive oxides for touchscreens or solar cells.^[7]

However, easy utilization of conductive oxides by ball milling—in a similar manner to how carbon-based cathode composites are prepared—did not yield a conductive composite,^[8] indicating that a carefully designed microstructure is necessary to successfully use conductive oxides as the electronically conductive additive in ASS-FIBs.

All types of carbon, which are typically used in electrode composites, Super P, carbon nanofibers, or carbon nanotubes, display a low percolation threshold due to their morphologies. Carbon nanofibers and nanotubes have a very large aspect ratio of length to diameter, which enables them to easily interconnect between powder particles. Super P consists of amorphous carbon particles with diameters between 30 and 40 nm,^[9] which allows them to occupy the pore space provided by solid electrolyte/active material particles. This large particle size ratio between active

T. H. Aalto, O. Clemens
Department of Chemical Materials Synthesis
Institute for Materials Science
University of Stuttgart
Heisenbergstraße 3, 70569 Stuttgart, Germany
E-mail: oliver.clemens@imw.uni-stuttgart.de

R. Talei, G. Schmitz
Department of Materials Physics
Institute for Materials Science, Synthesis
University of Stuttgart
Heisenbergstraße 3, 70569 Stuttgart, Germany
K. Küster
Max Planck Institute for Solid State Research
Heisenbergstraße 1, 70569 Stuttgart, Germany

 Supporting information for this article is available on the WWW under <https://doi.org/10.1002/batt.202500195>

 © 2025 The Author(s). *Batteries & Supercaps* published by Wiley-VCH GmbH. This is an open access article under the terms of the Creative Commons Attribution License, which permits use, distribution and reproduction in any medium, provided the original work is properly cited.

particles and carbon has been shown to also give rise to a low percolation threshold in powder mixtures.^[10]

Due to the small percolation threshold of nanoparticles, it was chosen to pursue the substitution of carbon in electrode composites by conductive F and Sb codoped SnO₂ nanoparticles, to deconvolute the effect of the conductive additive from the properties of the active material upon the cyclability of La₂(Ni/Co)O₄ in ASS-FIB cathode composites.

2. Experimental Section

2.1. Synthesis

2.1.1. Synthesis of Fluorine and Antimony-Doped Tin Oxide Nanoparticles

Fluorine and/or antimony (co)doped SnO₂ nanoparticles (FATO-NPs) were synthesized mechanochemically. Anhydrous tin chloride was chosen as a precursor, and Na₂CO₃ was added stoichiometrically as a reactant to achieve the reaction.



In addition, a large excess of NaCl was added as a dispersant. Antimony doping was achieved by substituting 5 mol.% of SnCl₂ for SbCl₃, while fluorine doping was carried out with the addition of a 1:1 ratio of NH₄F to metal ions. The mass of NaCl was chosen such that the total volume fraction of SnO after the reaction will be ≈3 vol%. All precursors were ball-milled for 2 h without intermediate rest in a 50 ml stainless steel ball milling jar with 100 g of 5 mm diameter stainless steel balls in an argon atmosphere. After milling, the powder was heated to 600 °C for 4 h with a heating/cooling rate of 3 °C min⁻¹ under 10 sccm pure oxygen flow to oxidize the SnO formed after ball milling to SnO₂ and decompose the ammonium fluoride to enable fluorination using the gaseous HF obtained in the process. The calcined powder mixture was then dispersed in deionized water to dissolve the sodium chloride, and the remaining solid was centrifuged out. After decanting the clear supernatant and adding fresh deionized water, the dispersion was sonicated using a Hielscher 200S ultrasonic probe to disperse the particles. This process was repeated until the supernatant after centrifuging was not clear, indicating dispersed particles. This supernatant was then kept as the sample while the sediment was discarded. This allows to separate contaminants formed by the abrasion of the ball milling jar and balls (see Figure S1, Supporting Information). For characterization and determination of the mass loading of the dispersion, 10 ml was dried in a petri dish at 100 °C, and the dry powder was weighed, used for X-ray diffraction and electrochemical impedance spectroscopy (EIS) to determine purity, crystallinity, and conductivity.

2.1.2. Battery Manufacturing

The solid electrolyte barium-doped lanthanum fluoride (La_{0.9}Ba_{0.1}F_{2.9}, 10% barium content) and anode composite of lead, lead fluoride, and carbon were synthesized as described elsewhere.^[11]

La₂NiO_{4+δ} was prepared according to Wissel et al.^[12] while La₂CoO_{4+δ} was synthesized as described by Nowroozi et al.^[3]

FATO-NPs-based cathode composites were prepared by first ball milling La_{0.9}Ba_{0.1}F_{2.9} and La₂(Ni/Co)O₄ in a 2:1 ratio at 250 rpm for 2 h using 10 pieces of 10 mm ZrO₂ balls in a 50 ml ZrO₂ jar in argon atmosphere. This powder was then added to a 100 mL round bottom flask with 20 ml of isopropanol, which was then sonicated in an ultrasonic bath for 10 min. To this flask, FATO-NPs in aqueous dispersion directly after sonication on a Hielscher 400S ultrasonic probe were added before the liquids were removed using a rotary evaporator. The volume of nanoparticle dispersion was chosen such that the final composite would be of a FATO-NPs:La_{0.9}Ba_{0.1}F_{2.9}:La₂(Ni/Co)O₄ 1:2:1 weight ratio. The composite was further dried at 170 °C in a vacuum for 15 h before being stored in a glovebox. Composites of FATO-NPs with exclusively La_{0.9}Ba_{0.1}F_{2.9} were prepared by the same method, using as-synthesized La_{0.9}Ba_{0.1}F_{2.9} instead of the mixture of La_{0.9}Ba_{0.1}F_{2.9} and La₂(Ni/Co)O₄ in a weight ratio of 75 wt% solid electrolyte and 25 wt% FATO-NPs.

A cathode composite of La₂(Ni/Co)O₄, La_{0.9}Ba_{0.1}F_{2.9}, and Super P was prepared by ball-milling 30 wt% La₂(Ni/Co)O₄, 60 wt% solid electrolyte, and 10 wt% Super P for 2 h at 250 rpm in a 50 ml ZrO₂ jar with 10 pieces of 10 mm zirconia balls in argon atmosphere. A composite of La_{0.9}Ba_{0.1}F_{2.9} and Super P was prepared by ball-milling 90 wt% solid electrolyte with 10 wt% Super P with the same parameters and ball milling equipment.

Batteries were assembled by pressing 5 mg of the cathode composite and 20 mg of the anode composite on either side of a 200 mg layer of the solid electrolyte at 460 MPa for 90 s. For FATO-based composites, a piece of gold leaf (24 carat) was then pressed onto the cathode surface to reduce the contact resistance between the pellet and the stainless-steel current collector. In case of the cells operated with applied stack pressure, gold leaf was also applied to the cathodes of the FATO- and the Super P-based cells to avoid corrosion of the current collector as observed in an earlier publication.^[11]

2.2. X-ray Diffraction

X-ray diffraction was carried out on a Rigaku SmartLab Diffractometer equipped with a HyPix-3000 detector and a Cu-K_α tube. No monochromator was used, but the detector had a Ni filter installed to absorb the Cu-K_β radiation. While FATO-NPs were measured in air, cathode composites and charged cell pellets were measured in airtight sample holders, which were sealed in an argon-filled glovebox. Rietveld analysis (including determination of lattice parameter changes as well as phase quantification) was carried out using the Bruker TOPAS Software.

2.3. Electron Microscopy

Bright-field transmission electron microscopy (TEM) images of the FATO-NPs were acquired using a Phillips FEG CM200 TEM with an accelerating voltage of 200 kV and equipped with a field emission gun. Samples were prepared by diluting 50 μl of the as-prepared FATO-NP dispersion in 2 ml of water and then placing one drop of

this dilute dispersion on a lacey-carbon coated copper TEM grid, which was subsequently dried at 100 °C. Particle sizes were analyzed using ImageJ by measuring the longest axis of the chosen particle.

Energy-dispersive X-ray spectroscopy (EDX) was carried out on a Tescan Vega (TS-5130MM) scanning electron microscope equipped with a NORAN System 7 (NSS212E) EDX detector.

2.4. Electrochemical Measurements

Electrochemical Impedance Spectroscopy, as well as Galvanostatic measurements, were conducted on a BioLogic VMP-300 potentiostat. Galvanostatic charging and cycling was conducted in Swagelok-type cells, which are assembled in an argon-filled glovebox and sealed using PTFE seals, which have been confirmed via helium-leak testing to show a leak rate smaller than 10^{-9} m bar l s $^{-1}$. Cycling with 50 MPa stack pressure was enabled using a modified Swagelok-cell design using polyether ether ketone (PEEK) tubes to constrain the cell pellet radially (see Figure S2, Supporting Information). Cycling with 180 MPa stack pressure was conducted in a hot-press as described elsewhere^[11] using PTFE liners in steel tubes for radial constraint. It has to be noted that the utilization of PTFE liners in steel tubes in the modified Swagelok-cell design for cycling with stack pressure resulted in poor reproducibility and mostly decreased cell performance (see Figure S10, Supporting Information). This is most likely due to the ductility of PTFE as compared to PEEK, which does not allow for good alignment of the current collector pins in this very compact form, while good alignment was ensured by the much longer PTFE liner in the hot-press for cycling at 180 MPa.

For the conductivity measurement of the FATO-NPs, the dried powder from 10 ml of nanoparticle dispersion was pressed into a 7.3 mm diameter pellet of approximate thickness of 1 mm at 460 MPa for 1 h before being sputtered with platinum. The conductivity was then determined via EIS between 1 MHz and 100 mHz.

2.5. Dynamic Light Scattering (DLS)

Before the particle size was determined via DLS, the nanoparticles were deagglomerated using a Hielscher 400S ultrasonic probe.

Afterwards, a single drop of the dispersion was diluted in 1.5 ml of deionized water, which was then used to determine the particle or agglomerate size using a Zen3600 Zetasizer from Malvern Panalytical.

2.6. X-Ray Photoelectron Spectroscopy

XPS was conducted using a Kratos Axis Ultra system with monochromatized Al $K\alpha$ X-rays. The pellets were mounted on the sample plate using an insulating double-sided sticky tape. The samples were transferred into the XPS system under inert gas without exposure to air. The charge neutralizer was used for charge compensation. For binding energy calibration, the Au $4f_{7/2}$ of the cycled samples was set to 84.0 eV.^[13] This results in a Ba $3d_{5/2}$ binding energy of 770.55 ± 0.05 eV. This value was used for the calibration of the binding energy of the Super P reference sample. Analysis of the data was performed using CasaXPS.^[14]

3. Results and Discussions

3.1. Characterization of FATO-NPs

Fluorine and antimony codoped nanoparticles have been prepared with a nominal F:Sn ratio of 1:1 and a nominal antimony doping level of 5%. EDX analysis (see Table S1 and Figure S3, Supporting Information) reveals a F:Sn ratio of 1:2, indicating a 50% loss of fluorine as gaseous HF in the synthesis. The antimony content of $\approx 7\%$ as determined by EDX analysis is close to the nominal doping level. The X-ray diffractogram (XRD) of FATO-NPs after drying is shown in Figure 1. The pattern could nicely be fitted with SnO_2 in the space group $P4_2/mnm$ and lattice parameters of $a = 4.7526(3)$ Å and $c = 3.1959(2)$ Å. After pressing into a pellet for 1 h at 460 MPa and sputtered with platinum, they showed a conductivity of 1.3×10^{-3} S cm $^{-1}$ (see Figure S4, Supporting Information).

Figure 2 shows a TEM micrograph of the FATO-NPs with the corresponding particle size distribution measured on 120 particles, as well as the particle size distribution measured by DLS after deagglomeration with a Hielscher 400S ultrasonic probe. The TEM image implies a particle size with a median value of

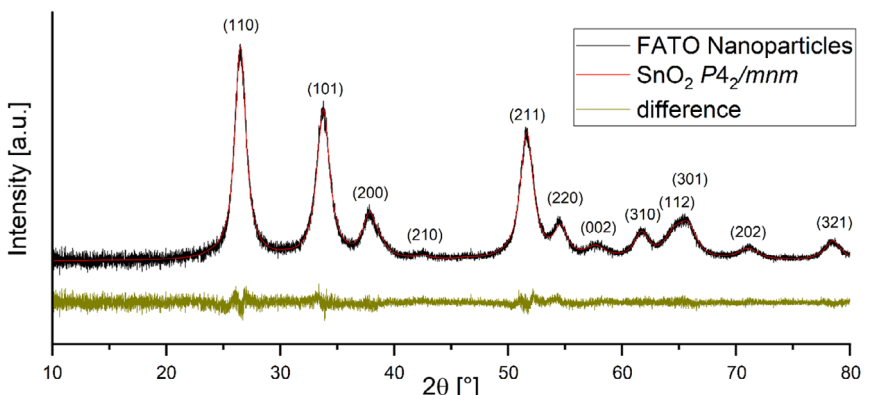


Figure 1. XRD of FATO-NP after drying.

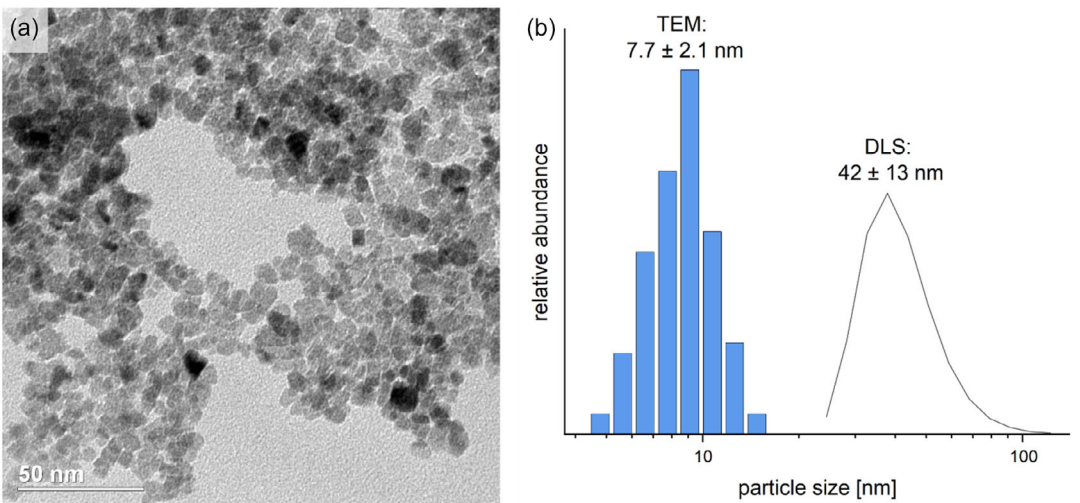


Figure 2. a) TEM micrograph of FATO-NP and b) particle size distribution by DLS and TEM for FATO-NPs.

7.7 nm, whereas the DLS measurement shows a median size of 42 nm, due to its sensitivity towards agglomeration. Even the size of agglomerates remaining after sonication is fully within the range of particle sizes expected for Super P,^[9] which should allow the conductive nanoparticles to form a percolating network at similar volume fractions as was previously used for Super P. This will be tested in section 3.2.1.

3.1.1. Electrochemical Stability of FATO-NPs

Cyclovoltammetry (CV) of the prepared conductive oxide nanoparticles was performed in a cell of the composition $\text{La}_{0.9}\text{Ba}_{0.1}\text{F}_{2.9}/\text{FATO-NPs}-\text{La}_{0.9}\text{Ba}_{0.1}\text{F}_{2.9}-\text{Pb}/\text{PbF}_2/\text{C}$ as well as on a cell with a cathode made of a composite of $\text{La}_{0.9}\text{Ba}_{0.1}\text{F}_{2.9}$ and Super P. Both cells had gold leaf pressed on top of the cathode side for better comparability, the resulting voltammograms are shown in Figure 3.

The CVs of the FATO-NPs composites show a significant difference between the first and subsequent cycles. The first cycle shows an irreversible cathodic peak between 1–1.5 V against Pb/PbF_2 , likely due to the oxidation of not fully oxidized Sn^{2+} or Sb^{3+}

species. Above 1.7 V against Pb/PbF_2 , another much larger oxidative peak starts. While the large cathodic current above 2.2 V against Pb/PbF_2 can be attributed to the fluorination of gold (compare Figure S5, Supporting Information), the current between 1.7 and 2.2 V must originate from other side reactions including the FATO-NPs like substitutive fluorination by oxygen evolution from oxidation of lattice oxide ions. After the first cathodic scan, the FATO-NPs show a small reversible current around 0–1 V against Pb/PbF_2 , which remains consistent through subsequent cycles, indicating a stable reversible capacity in the range of 3–5 mAh g⁻¹ (see Figure S6, Supporting Information). The oxidative current above 1.7 V also remains unchanged through all five cycles.

The CV of Super P shows an oxidative peak of nearly 15 μA in the first cycle around 1.5 V against Pb/PbF_2 with no corresponding anodic peak. This peak is due to irreversible fluorination of carbon as previously discussed by Nowroozi et al.^[4] In subsequent cycles, the peak current decreases continuously, as well as the current due to gold fluorination above 2.3 V against Pb/PbF_2 . The continuous decrease in the peak current can be either interpreted as a saturation of the carbon fluorination by

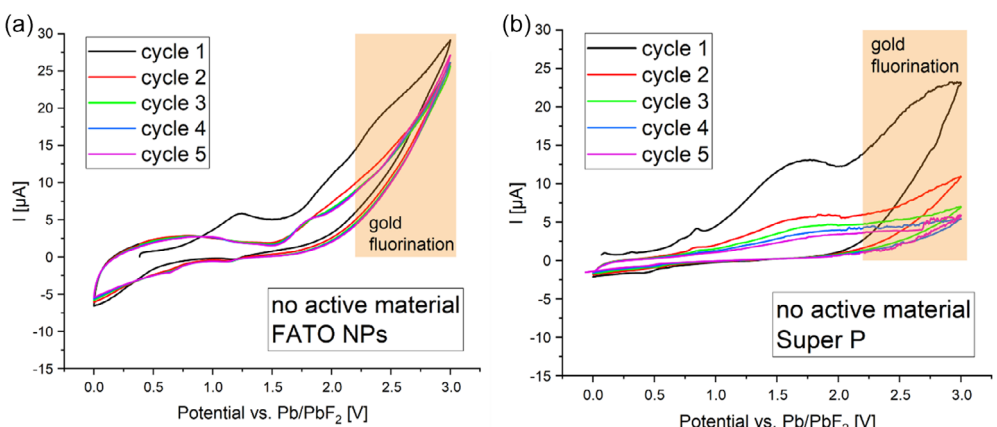


Figure 3. Cyclovoltammogram of a) FATO-NPs, and b) Super P against Pb/PbF_2 with a scan rate of 0.1 mV s⁻¹.

a passivating effect or as a deterioration of the conductivity of the cathode composite, due to carbon fluorination.

The comparison of the CVs of Super P and FATO-NPs shows that FATO-NPs are able to form a stable conductive matrix, as judged by the stable performance in the cyclovoltammogram from the second cycle onward, not showing decreasing currents which would imply a deterioration of the additive's conductivity, as is the case for Super P.

3.2. Comparison of FATO-Based Composites to Carbon-Based Composites

3.2.1. Galvanostatic Fluorination

Figure 4 compares the charging curves and corresponding XRDs (after mostly scratching off the gold current collector) of $\text{La}_2(\text{Ni}/\text{Co})\text{O}_4$ FATO-based composites and Super P-based composites charged to 1.7 V. For both active materials, the FATO-based composites show a slightly higher plateau potential compared to the Super P-based composites, due to the lower conductivity of the FATO-NPs. While this difference is about 200 mV for La_2CoO_4 , it is only about 100–150 mV for La_2NiO_4 .

Remarkably, for La_2CoO_4 an increase in the cell's potential can be observed very close to the theoretical capacity of 133 mAh g^{-1} of the active material La_2CoO_4 for the FATO-based composite, reaching the cut off potential below 170 mAh g^{-1} , while the Super P-based composite shows no distinct feature around this capacity value. Therefore, the final capacity until the cut off

voltage of 1.7 V is reached is much larger for the Super P-based composite. This displays that irreversible fluorination of the conductive additive is massively reduced in the FATO-based composites and agrees with the previous findings that C-fluorination is a side reaction during the first oxidative fluorination. This can also clearly be seen by comparing the initial charging capacities of FATO-NPs and Super P in a $\text{La}_{0.9}\text{Ba}_{0.1}\text{F}_{2.9}$ composite without any active material (see Figure S6, Supporting Information).

For La_2NiO_4 , the FATO-based composite also reaches the cut off potential much closer to the theoretical capacity than the Super P-based composite, again demonstrating the higher oxidative stability of the FATO-NPs in comparison to carbon. However, with about 220 mAh g^{-1} , the FATO-based composite of La_2NiO_4 takes significantly more capacity to reach 1.7 V than the FATO- La_2CoO_4 composite. This implies another, unknown kind of side reaction taking place with La_2NiO_4 specifically.

Although the charging capacity is lower for the FATO-based composites, Rietveld refinements of the charged cells reveal that similar degrees of fluorination have been achieved in both composites. For, La_2CoO_4 full conversion into the monoclinic fluorinated phase was achieved, as reported before by Nowroozi et al.^[3] showing that the cathode composites prepared as described in Section 2.1.2 allow all particles of the chosen active material to participate in the electrochemical reaction and that the particle size obtained by ball milling is sufficiently small to fully fluorinate the respective powder particles.

For La_2NiO_4 , Nowroozi et al. did not report a full conversion to the fluorinated phase, as they could only achieve $\approx 70\%$

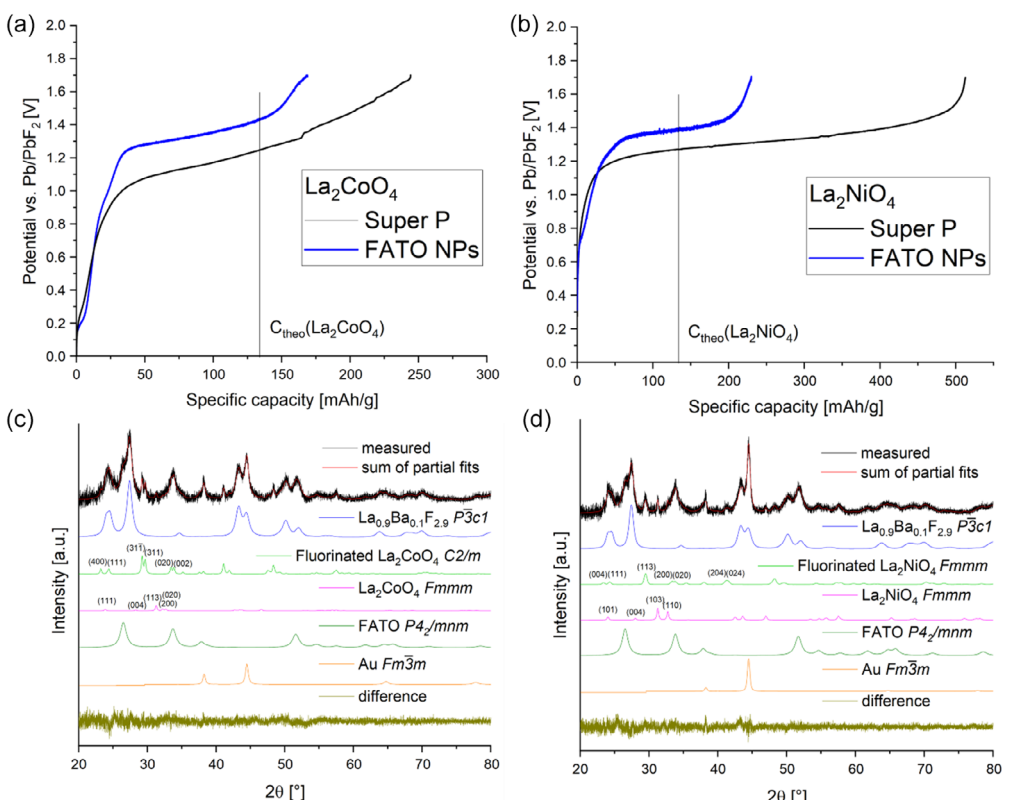


Figure 4. Charging curves of a) La_2CoO_4 and b) La_2NiO_4 in FATO- and Super P-based composites, and the corresponding XRDs of the FATO-based composites for c) La_2CoO_4 and d) La_2NiO_4 .

conversion to the fluorinated phase with a c-lattice parameter of $\approx 15.25 \text{ \AA}$.^[4] A similar observation is present for La_2NiO_4 in a FATO-based composite, as only $\approx 60\%$ of the active material was fully fluorinated. Even though the remaining La_2NiO_4 in the space group $I4/mmm$ shows an expansion of the c-axis ($c = 12.73 \text{ \AA}$) as compared to the pristine material ($c = 12.68 \text{ \AA}$), which is indicative of an oxidative fluorination as also reported by Nowroozi et al.^[4] Despite the fact that not all the La_2NiO_4 present in the composite could be fully fluorinated, all powder particles participate in the electrochemical reaction, also for this composite.

Using the weight fractions as described in the experimental section, all composites have equal volume fractions of solid electrolyte:active material:conductive additive of 54:23:23 vol%. As the composition of the Super P-based composites remains unchanged from those used in earlier publications on FIBs,^[3–6,11,15] the successful electrochemical fluorination of La_2CoO_4 and La_2NiO_4 in FATO-NP-based cathode composites shows that the preparation method by cosonicating all components of the composite ensures percolation networks which enable access all to particles of the active material for electrochemistry.

3.3. Long Term Cycling

Figure 5 shows cycling data of La_2NiO_4 and La_2CoO_4 in FATO-NP and Super P-based composites at different stack pressures. The corresponding charge-discharge curves shown in Figure S7 and S8, Supporting Information. The comparison of the cyclic performance without stack pressure already shows that FATO-NPs are performing significantly better as a conductive additive as compared to Super P. While both Super P-based cells failed before reaching 10 cycles, the FATO-NP based cells cycled with much better stability, still supplying significant discharge capacities of $\approx 20 \text{ mAh g}^{-1}$ after 50 cycles for La_2CoO_4 and La_2NiO_4 , respectively. However, the maximum discharge capacity for La_2NiO_4 was 60 and 65 mAh g^{-1} for La_2CoO_4 , which is only about half of the theoretical capacity of 133 mAh g^{-1} for both materials. Further, the cells were only able to support this capacity for a few cycles before starting to fade. It has to be mentioned that due to the absence of stack pressure, the difference in performance is most likely also affected by microstructural differences, not only due to different amounts of side reactions.

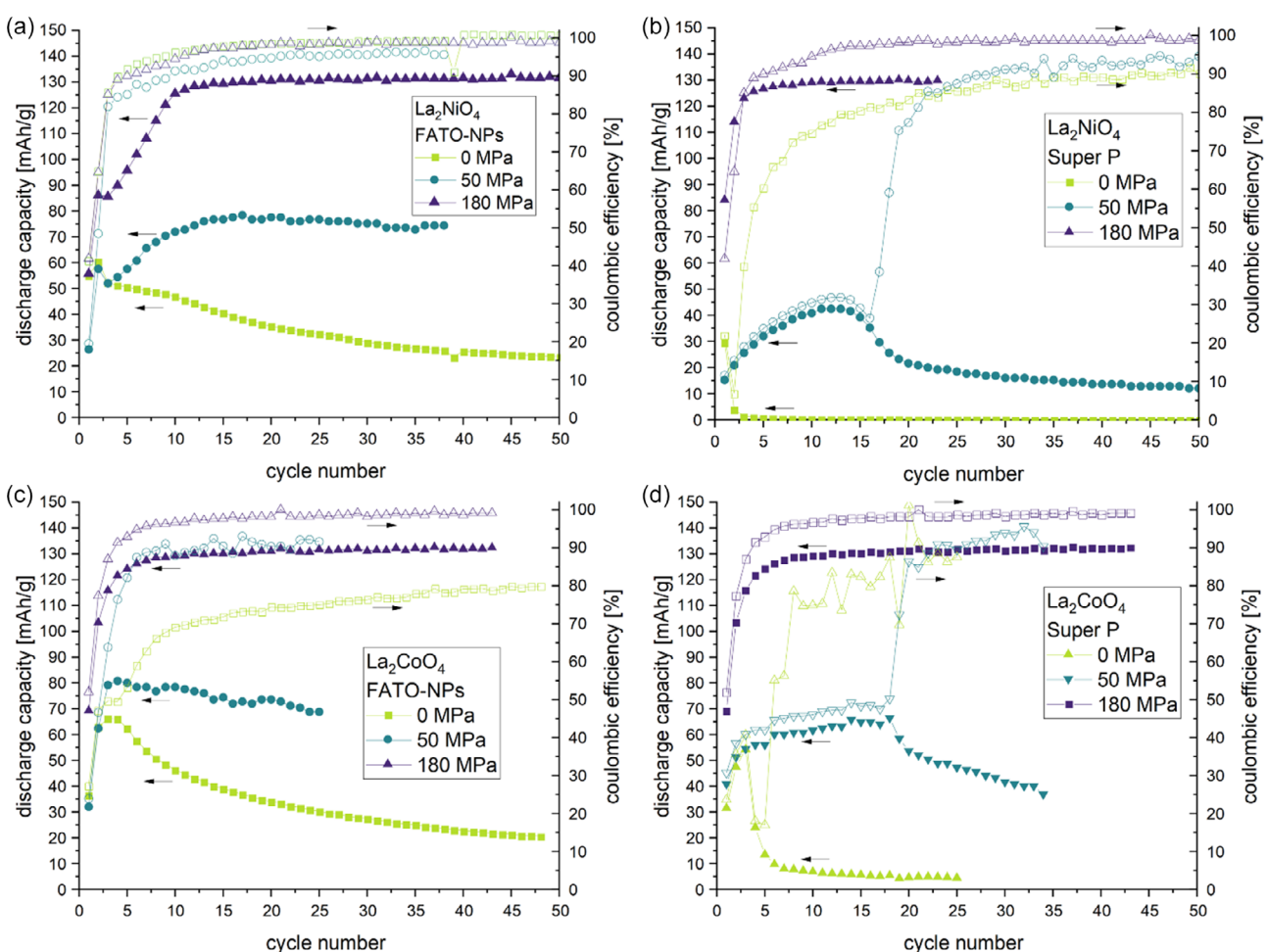


Figure 5. Discharge capacities and coulombic efficiencies of La_2NiO_4 in a) FATO-NPs or b) Super P-based composites and c) La_2CoO_4 in FATO-NPs and d) Super P-based composites at 180, 50 MPa, and no stack pressure (0 MPa). Discharge capacities are represented by full symbols while coulombic efficiencies are displayed by hollow symbols. All cells have been cycled with a charging cut off of 133.4 mAh g^{-1} . The different numbers of cycles for which the cells at 180 MPa have been tested are due to device availability and the time-intensiveness of extended low C-rate cycling.

Upon application of 50 MPa stack pressure, $\text{La}_2(\text{Ni}/\text{Co})\text{O}_4$ in a FATO-based composite is able to provide stable discharge capacities of $\approx 70 \text{ mAh g}^{-1}$ with high coulombic efficiency $>90\%$. For the Super P-based composite, the discharge capacity is steadily increasing for the first 10 cycles for La_2NiO_4 and 18 cycles for La_2CoO_4 , after which it drops sharply and continues to decay to about 10 mAh g^{-1} after 50 cycles. Until the sharp drop in capacity is reached, the coulombic efficiency is low, due to the high charging capacity of 133.4 mAh g^{-1} (see Figure S7 and S8, Supporting Information). In the following cycles, the charging capacity is much smaller due to a strong increase in overpotentials, resulting in higher coulombic efficiencies.

At a stack pressure of 180 MPa, both La_2NiO_4 and La_2CoO_4 were able to cycle with high coulombic efficiency at the theoretical capacity of 133.4 mAh g^{-1} after some initial activation cycles, far surpassing the discharge capacity and cyclic stability which have been reported before for these materials.^[3,4] This stable discharge capacity was independent of the conductive additive used. This revelation highlights again the importance of stack pressure for solid-state batteries, while it also shows that intercalation cathodes for fluoride ion batteries can operate at high potential, high capacity, and high coulombic efficiency even if

conductive carbon additives are used. This is in stark contrast to previous assumptions.

Some small differences in the charging behavior and the resulting energy efficiencies are visible between the different cells. Interestingly, the $\text{La}_2\text{NiO}_4/\text{FATO-NPs}$ cells showed a drop in the charging capacity after two cycles, after which the charging capacity again increased gradually. This phenomenon occurred independently of stack pressure. While the drop in charging capacity most likely originates from reduced side reactions leading to the cell reaching the cut off potential before reaching the cut off capacity, the activation mechanism leading to the increase in charge and discharge capacities after the second cycle is unknown. Only the correlation between dropping overpotentials for both the charge and discharge cycles and increasing charge and discharge capacities clearly shown in Figure S8, Supporting Information.

The capacity decay of the FATO-NPs based cells with 0 MPa and 50 MPa stack pressure is most likely affected by contact loss due to volume change. This is supported by the much more stable cyclic performance upon increasing the stack pressure to 180 MPa. While contact loss certainly also affects the Super P-based cells at 0 and 50 MPa stack pressure, carbon fluorination

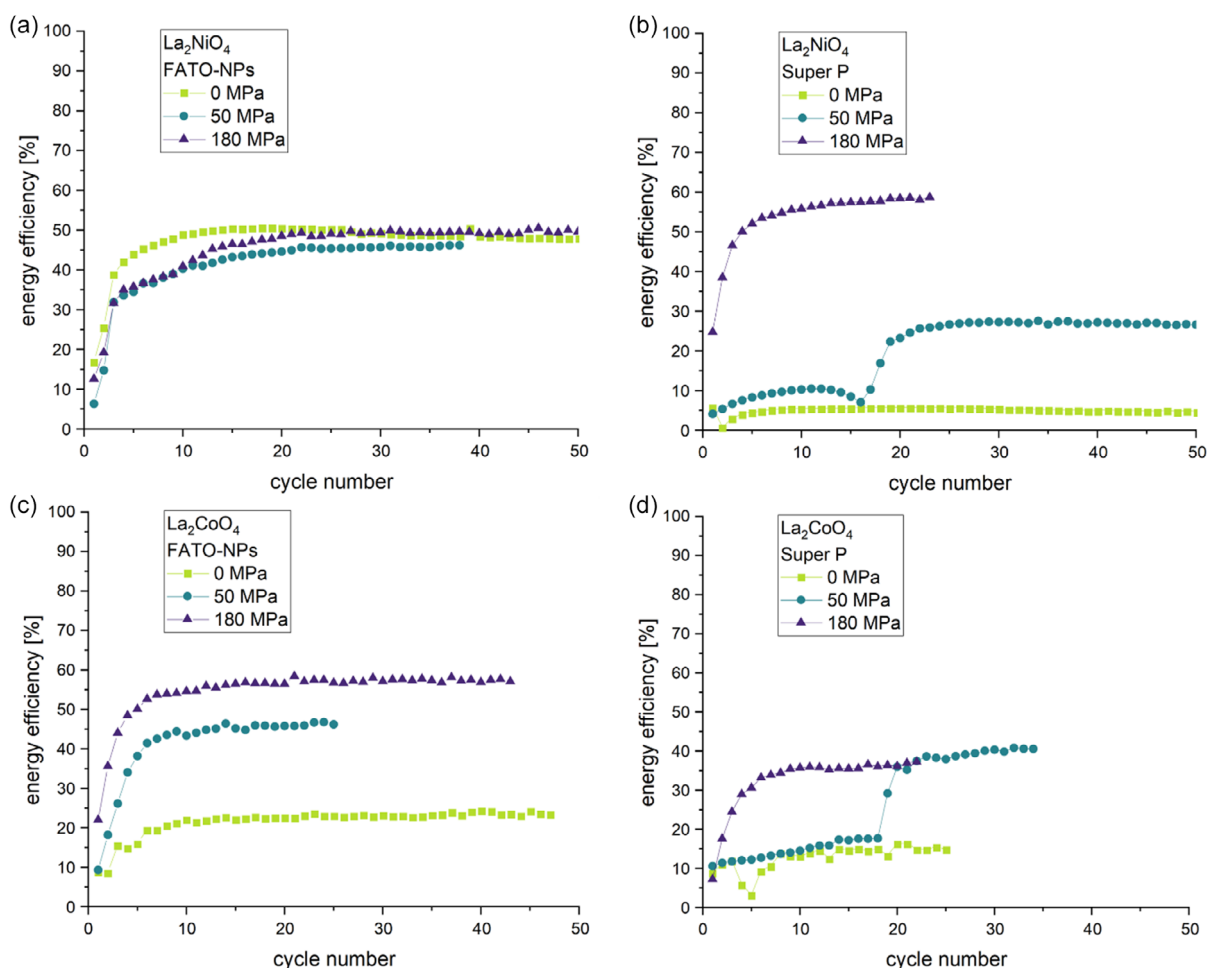


Figure 6. Energy efficiency of La_2NiO_4 in a) FATO-NPs and b) Super P-based composites and La_2CoO_4 in c) FATO-NPs and d) Super P-based composites at different stack pressures.

affects the cyclability. This is apparent due to low coulombic efficiency, increasing overpotentials, and overall lower cyclic stability as compared to the FATO-NPs-based cells at the same stack pressure.

The energy efficiency of $\text{La}_2(\text{Ni}/\text{Co})\text{O}_4$ cycled at different stack pressures, which was obtained by integrating the cycling curves, is displayed in Figure 6. For all composites except the $\text{La}_2\text{NiO}_4/\text{FATO-NPs}$ composite, the energy efficiency is improved by applying stack pressure. This is again due to a reduction of overpotentials by improving interparticle contact. The carbon-based composites both show a phenomenon after ≈ 17 cycles at 50 MPa, where the energy efficiency suddenly increases. This correlates with drastically smaller charging capacities due to reaching the voltage cutoff, thereby also reducing the charging energy.

The $\text{La}_2\text{NiO}_4/\text{FATO-NPs}$ composite shows an energy efficiency of $\approx 40\%-50\%$ after 10 cycles, mostly independent of the applied stack pressure.

When cycled at 180 MPa, Super P was able to provide lower overpotentials than FATO-NPs for La_2NiO_4 , and therefore, higher energy efficiency, while the opposite is the case for La_2CoO_4 , where the FATO-based composite resulted in better energy efficiency. This demonstrates that even though Super P did not inhibit good cyclic stability, carbon fluorination did most likely take place, and thereby affect the overpotential. The extend of carbon fluorination also seems to be different for La_2NiO_4 and La_2CoO_4 , where La_2NiO_4 shows to have better compatibility with carbon additives, similar to what was shown before by Nowroozi et al. for cycling with limited cut off capacities at ambient pressure.^[3,4] To improve the understanding of the role of carbon, XPS spectra of the cathode layers after cycling have been recorded to compare the degree of carbon fluorination. Figure 7 shows the C 1s XPS spectra of the cathode sides of both Super P-based cells after completing 23 cycles at 180 MPa, along with a pristine reference sample of Super P ball-milled with $\text{La}_{0.9}\text{Ba}_{0.1}\text{F}_{2.9}$.

Super P shows a shoulder around 282 eV, which is absent for both spectra of the cycled cells. Additionally, the peak is

slightly shifted toward higher binding energies for the La_2CoO_4 sample and the La_2NiO_4 sample after cycling. This shift and the elimination of the low binding energy shoulder indicate that a small degree of carbon fluorination did take place. Especially, since the C 1s spectrum of the $\text{La}_2\text{CoO}_4/\text{Super P}$ cell is shifted slightly larger than that of the $\text{La}_2\text{NiO}_4/\text{Super P}$ cell, it can be assumed that carbon fluorination was more expressed for the La_2CoO_4 sample, even though the difference is small. Unfortunately, the spectrum of Super P is considerably widened. Since this is not the case for other spectra like the Ba 3d and Au 4f spectra (Figure S9, Supporting Information), it cannot be considered a measurement artifact, therefore, a more precise interpretation of the binding energy for a detailed determination of the degree of carbon fluorination has to be avoided.

Even more striking is the comparison of these shifts in binding energy to those published by Nowroozi et al.^[4] and Wissel et al.^[6] which both show much larger shifts in binding energy of 0.5–0.8 eV toward higher values after charging the cathode composites. This difference highlights the suppression of carbon fluorination by applying high stack pressures, which was indicated to already in an earlier publication^[11] and is now supported by the much smaller increase in binding energy of the C 1s XPS spectra of the cells cycled at 180 MPa as compared to the data published by Nowroozi et al. where no stack pressure was applied.

While similar discharge capacities with high cyclic stability have been reported before for materials such as $\text{Sr}_3\text{Fe}_2\text{O}_5\text{F}_2$ ^[16] or $\text{La}_{1.2}\text{Sr}_{1.8}\text{Mn}_2\text{O}_{7-\delta}\text{F}_x$,^[17] both of these materials were discharged to -1.5 V versus Pb/PbF_2 , which sets the data presented in this work apart, since all capacity was able to be provided in a well-expressed plateau at ≈ 0.6 V versus Pb/PbF_2 .

4. Conclusions and Outlook

This study presents the possibility of eliminating carbon-based side reactions in ASS-FIBs by manufacturing carbon-free cathode composites using FATO-NPs instead of carbon as the conductive additive.

FATO-based composites showed much lower irreversible charging capacity in the first cycle when charged to 1.7 V against Pb/PbF_2 . At a stack pressure of 50 MPa, FATO-based composites outperformed those based on Super P significantly, emphasizing the importance of eliminating side reactions in low stack pressure conditions, which are more viable for application than conditions of higher stack pressure.^[18]

Both types of conductive additives were able to provide good coulombic efficiency at high discharge capacities at 180 MPa stack pressure. Contrary to previous assumptions, this shows that conductive-carbon additives are well-suited if high stack pressure is applied, which drastically limits the degree of carbon fluorination as was shown by XPS. These results demonstrate the potential of $\text{La}_2(\text{Ni}/\text{Co})\text{O}_4$ as intercalation-based high-voltage cathode materials for fluoride ion batteries.

Even though the substitution of carbon for FATO-nanoparticles reduced irreversible side reactions in the first charging cycles

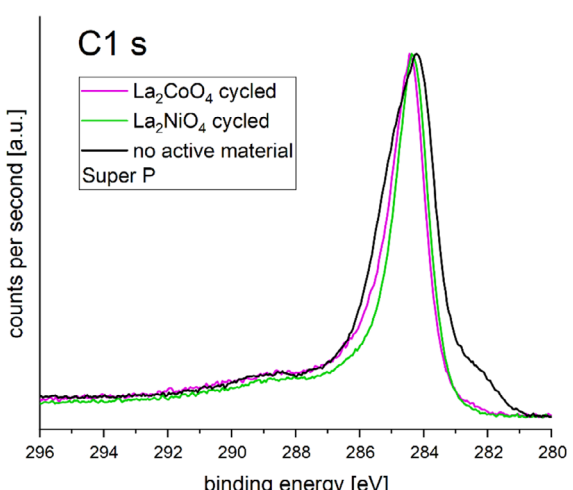


Figure 7. C 1s XPS spectra of the two Super P-based cells cycled at 180 MPa along with a reference sample of a ball-milled mixture of Super P and $\text{La}_{0.9}\text{Ba}_{0.1}\text{F}_{2.9}$, which has not been subject to electrochemistry. All spectra are normalized to the maximum intensity.

drastically, some side reactions still remained. The nature of the remaining side reactions will certainly be investigated in future research.

Acknowledgements

The authors express their gratitude to Hong Chen for helpful discussions during the scope of this work.

Open Access funding enabled and organized by Projekt DEAL.

Conflict of Interest

The authors declare no conflict of interest.

Author Contributions

Tommi Hendrik Aalto: conceptualization (lead); investigation (lead); writing—original draft (lead); writing—review and editing (lead). **Roham Talei:** data curation (supporting); investigation (supporting). **Kathrin Küster:** data curation (supporting). **Guido Schmitz:** resources (supporting); validation (supporting). **Oliver Clemens:** conceptualization (supporting); supervision (lead); writing—original draft (supporting); writing—review and editing (supporting).

Data Availability Statement

The data that support the findings of this study are available from the corresponding author upon reasonable request.

Keywords: conducting materials • fluoride ion batteries • nanoparticles • percolation • solid-state batteries

- [1] F. Gschwind, G. Rodriguez-Garcia, D. J. S. Sandbeck, A. Gross, M. Weil, M. Fichtner, N. Hörmann, *J. Fluorine Chem.* **2016**, *182*, 76.
- [2] M. A. Nowroozi, I. Mohammad, P. Molaiyan, K. Wissel, A. R. Munnangi, O. Clemens, *J. Mater. Chem. A* **2021**, *9*, 5980.
- [3] M. A. Nowroozi, S. Ivlev, J. Rohrer, O. Clemens, *J. Mater. Chem. A* **2018**, *6*, 4658.

- [4] M. A. Nowroozi, K. Wissel, M. Donzelli, N. Hosseinpourkahvaz, S. Plana-Ruiz, U. Kolb, R. Schoch, M. Bauer, A. M. Malik, J. Rohrer, S. Ivlev, F. Kraus, O. Clemens, *Commun. Mater.* **2020**, *1*, 27.
- [5] M. A. Nowroozi, K. Wissel, J. Rohrer, A. R. Munnangi, O. Clemens, *Chem. Mater.* **2017**, *29*, 3441.
- [6] K. Wissel, R. Schoch, T. Vogel, M. Donzelli, G. Matveeva, U. Kolb, M. Bauer, P. R. Slater, O. Clemens, *Chem. Mater.* **2021**, *33*, 499.
- [7] a) A. Adjimi, M. L. Zeggar, N. Attaf, M. S. Aida, *J. Cryst. Process Technol.* **2018**, *08*, 89; b) L. M. Cukrov, T. Suzuki, P. G. McCormick, *Scr. Mater.* **2001**, *44*, 1787; c) N. Haddad, Z. Ben Ayadi, H. Mahdhi, K. Djessas, *J. Mater. Sci.: Mater. Electron.* **2017**, *28*, 15457; d) M. John Silvester Raju, S. S. Bhattacharya, *Mater. Today: Proc.* **2018**, *5*, 10097; e) A. S. Mohd Hanif, W. K. Lau, F. Mohamad, W. S. Wan Zaki, M. K. Ahmad, *Appl. Mech. Mater.* **2015**, *773–774*, 632; f) V. Senthilkumar, P. Vickraman, R. Ravikumar, *J. Sol-Gel Sci. Technol.* **2009**, *53*, 316; g) A. Stadler, *Materials* **2012**, *5*, 661; h) S. Wu, S. Yuan, L. Shi, Y. Zhao, J. Fang, *J. Colloid Interface Sci.* **2010**, *346*, 12; i) H. Yang, Y. Hu, A. Tang, S. Jin, G. Qiu, *J. Alloys Compd.* **2004**, *363*, 276.
- [8] M. A. Nowroozi, *On the Development of Intercalation-Based Cathode Materials for All-Solid-State Fluoride Ion Batteries*, Technische Universität Darmstadt, Darmstadt, Germany **2020**.
- [9] a) I. Cho, J. Choi, K. Kim, M.-H. Ryou, Y. M. Lee, *RSC Adv.* **2015**, *5*, 95073. b) R. M. Gnanamuthu, C. W. Lee, *Mater. Chem. Phys.* **2011**, *130*, 831.
- [10] D. He, N. N. Ekere, *J. Phys. D: Appl. Phys.* **2004**, *37*, 1848.
- [11] H. Chen, T. Aalto, V. Vanita, O. Clemens, *Small Struct.* **2024**, *5*, 2300570.
- [12] K. Wissel, J. Heldt, P. B. Groszewicz, S. Dasgupta, H. Breitzke, M. Donzelli, A. I. Waidha, A. D. Fortes, J. Rohrer, P. R. Slater, G. Buntkowsky, O. Clemens, *Inorg. Chem.* **2018**, *57*, 6549.
- [13] J. F. Moulder, W. F. Stickle, P. E. Sobol, K. D. Bomben, *Handbook of X-ray Photoelectron Spectroscopy* (Ed: J. Chastain), Perkin-Elmer Corporation, Eden Prairie, USA **1992**.
- [14] N. Fairley, V. Fernandez, M. Richard-Plouet, C. Guillot-Deudon, J. Walton, E. Smith, D. Flahaut, M. Greiner, M. Biesinger, S. Tougaard, D. Morgan, J. Baltrusaitis, *Appl. Surf. Sci. Adv.* **2021**, *5*, 100112.
- [15] M. A. Nowroozi, B. de Laune, O. Clemens, *ChemistryOpen* **2018**, *7*, 617.
- [16] Y. Wang, T. Takami, Z. Li, K. Yamamoto, T. Matsunaga, T. Uchiyama, T. Watanabe, H. Miki, T. Inoue, H. Iba, U. Mizutani, H. Sato, K. Maeda, H. Kageyama, Y. Uchimoto, *Chem. Mater.* **2022**, *34*, 10631.
- [17] H. Miki, K. Yamamoto, H. Nakaki, T. Yoshinari, K. Nakanishi, S. Nakanishi, H. Iba, J. Miyawaki, Y. Harada, A. Kuwabara, Y. Wang, T. Watanabe, T. Matsunaga, K. Maeda, H. Kageyama, Y. Uchimoto, *J. Am. Chem. Soc.* **2024**, *146*, 3844.
- [18] a) X. Gao, B. Liu, B. Hu, Z. Ning, D. S. Jolly, S. Zhang, J. Perera, J. Bu, J. Liu, C. Doerrer, E. Darnbrough, D. Armstrong, P. S. Grant, P. G. Bruce, *Joule* **2022**, *6*, 636; b) H. Xu, S. Yang, B. Li, *Adv. Energy Mater.* **2024**, *14*, 2303539; c) D. H. S. Tan, Y. S. Meng, J. Jang, *Joule* **2022**, *6*, 1755.

Manuscript received: April 11, 2025

Revised manuscript received: May 19, 2025

Version of record online: